Article:

Flint, T.F., Anderson, M.J., Akrivos, V. et al. (2022) A fundamental analysis of factors affecting chemical homogeneity in the laser powder bed fusion process. International Journal of Heat and Mass Transfer, 194. 122985. ISSN: 0017-9310

https://doi.org/10.1016/j.ijheatmasstransfer.2022.122985

International Journal of Heat and Mass Transfer 194 (2022) 122985

Contents lists available at ScienceDirect

International Journal of Heat and Mass Transfer

journal homepage: www.elsevier.com/locate/hmt

A fundamental analysis of factors affecting chemical homogeneity in the laser powder bed fusion process

T.F. Flint[a,b,*], M.J. Anderson[c], V. Akrivos[a], M.J. Roy[d,b], J.A. Francis[a], A. Vasileiou[a], M.C. Smith[a]

[a] Dalton Nuclear Institute, The University of Manchester, Manchester, UK
[b] Department of Materials, Henry Royce Institute, University of Manchester, M13 9PL, UK
[c] Department of Materials Science and Engineering, The University of Sheffield, Sheffield, UK
[d] Department of Mechanical, Aerospace and Civil Engineering, University of Manchester, M13 9PL, UK

ARTICLE INFO

Article history:
Received 24 October 2021
Revised 22 April 2022
Accepted 27 April 2022
Available online 7 May 2022

Keywords:
Volume of fluid
Thermal fluid dynamics
Heat transfer
Vaporisation
Laser powder bed fusion
Additive manufacturing

ABSTRACT

In this work a novel mathematical framework, that fully describes the fusion and vapourisation state transitions in multi-component systems, has been applied to assist in understanding the fundamental mechanisms of defect formation and chemical homogenisation in the laser powder bed fusion process (L-PBF). Specifically, the role of vapourisation and condensation of the multi-component metallic substrate is investigated to determine the importance of properly capturing the state transitions when understanding the substrate evolution. The framework is applied to a ternary metallic system; it is revealed that entrained vapour bubbles in chemically dissimilar flows promote greater homogenisation during the condensation and collapse of these bubbles when compared to non-condensing phases. It is further shown that as the laser power density is increased, there is a greater tendency for preferential element evaporation of the lighter elements; this preferential element evaporation is quantified numerically for the first time, and shown to be a non-linear function of power density.

1. Introduction

Laser powder bed fusion (L-PBF) offers a novel route for the fabrication of components in a variety of industries including aerospace, automotive and nuclear. In the powder bed fusion process, thin layers of powder are deposited onto a build plate and a focused energy source (laser or electron beam) is used to consolidate the powder. When one layer is completed, a new layer of powder is applied, and the process is repeated until a 3D part is produced [1]. Recently, the viability of multi-material functionally additive manufactured (MM-FGAM) components has been demonstrated, whereby different properties can be attained by alloying components in-situ during processing [2]. In these scenarios, heterogeneous mixing between the materials in the fluid state occurs and the alloy composition varies throughout the component.

Metallic components fabricated through L-PBF are susceptible to inherent defects due to the nature of the process. These can include: sub-surface porosity, poor surface finish, high levels of residual stress or distortion, significant chemical segregation, and potentially undesirable microstructure formation [3]. The high energy density nature of the heat source used in L-PBF causes localised melting and, when the power density is sufficient, vapourisation of the metallic substrate [4]. The vapour column that is generated by the heat source is referred to as the thermo-capillary, or a 'keyhole'. With sufficient and sustained power density of the applied heat source, multi-component systems can experience preferential elemental evaporation [5–7]. The stability of the thermo-capillary structure is determined by the complex interplay between recoil forces at the liquid-vapour interface, gravity and surface tension, with all of the preceding strongly dependent on local temperatures [8–10]. Once the heat source is extinguished, the collapse of the thermo-capillary and condensation of the various vapourised metallic components is a route for significant porosity formation - particularly if the vapour bubbles are caught by the progressing solidification interface prior to complete condensation. Furthermore, the complex mixing in the fluid state governs the degree of chemical heterogeneity in the substrate following solidification. Therefore, understanding the coupled and highly transient thermal, compositional, and momentum fields generated in metallic substrates during these high energy density processes is key to optimising

---

* Corresponding author at: Dalton Nuclear Institute, The University of Manchester, Manchester, UK.
E-mail address: Thomas.Flint@manchester.ac.uk (T.F. Flint).

https://doi.org/10.1016/j.ijheatmasstransfer.2022.122985

such processes, and material systems, for next generation applications [11–16].

The high temperatures and highly transient nature of the thermo-capillary formation and molten pool behaviour make it difficult to experimentally observe the flow behaviour of the metallic powder and substrate system [15,17,18]. Therefore, mathematical modelling of these high energy density L-PBF processes offers unique opportunities to understand the evolution of the powder substrate and will help predict the types of powder size distributions, and heat source characteristics that will lead to improved properties within fabricated components. Many frameworks exist for modelling the thermal-fluid dynamics of L-PBF processes [12,13,19–23]. However, the majority of the approaches in the literature do not account for the volumetric change associated with vapourisation and condensation state transitions, assuming the divergence of the velocity field is zero. It is the effect of the volumetric dilation of the vapourising substrate, exerting a recoil pressure at the liquid/vapour interface, that largely stabilises the thermo-capillary. This renders frameworks neglecting these density changes during vapourisation/condensation in-capable of capturing the physical mechanisms behind thermo-capillary evolution and stability - instead relying on phenomenological treatments of the recoil pressure [24]. Similarly, approaches utilising a simple volume-of-fluid description of the domain to differentiate between the metallic solid and vapour phases do not capture the multi-component nature of the substrate, which is normally an alloy comprised of multiple chemical species, in these approaches dissimilar metal systems, preferential element evaporation and other compositional effects cannot be considered [11,25,26].

Recently a mathematical formulation has been presented that fully captures the volumetric dilation due to the vapourisation and condensation transitions within a multi-component system [27]. This framework extends the traditional volume-of-fluid treatment to multi-component transport incorporating diffusive and advective fluxes between the species, in addition to transition source terms for condensation and vapourisation; the novelty in this approach lies in decomposing each chemical component into two phases, a condensed phase and vapourised phase, with the vapourisation/condensation transition treated explicitly between these two phases. This permits the nuances of the multi-component vapourisation to be fully captured in the presented approach, such as the preferential element loss that is observed in L-PBF, and other high energy density, processes [5]. Another approach has been presented that is similar [28], but does not explicitly capture the transition between condensed and vapourised states for each component, so the effect of how the volumetric dilation is partitioned into each components phase space is lost in this approach [28]. In the approach presented in this work the multi-component transitions are fully captured in a mass conservative framework. The combination of the multi-component transport equation, the momentum conservation equation and an energy transport equation form a fully coupled system of equations that describe multi-component alloy systems experiencing fusion and vapourisation state changes. The model considers the effect of surface tension, the dependence of surface tension on temperature (often referred to as Marangoni forces), buoyancy, and recoil velocity on the formation of the thermo-capillary. A Gaussian surface representation of a power beam heat source, applicable to both laser and electron beams is utilized in the energy equation. This is in contrast to phenomenological heat input descriptions used elsewhere for similar end purposes [25], reducing the need for excessive model calibration.

In the present work, a robust mathematical framework proposed elsewhere, [27], is applied to study the L-PBF process with particular attention paid to the elemental losses experienced by the substrate. This novel approach explicitly captures the multi-component nature of the metallic substrate. Furthermore, this modelling approach captures the complex fluid-vapour dynamics due to both fusion and vapourisation state transitions and is mass conservative. Initially the mathematical framework is used to investigate the behaviour of vapour bubble condensation within a Rayleigh-Taylor (R-T) instability to glean fundamental insights into the role of vapour-bubble collapse on the mixing dynamics in a dissimilar, ternary, liquid-metal system. This framework is then applied to an L-PBF process where two types of binary-alloy powder are mixed and then melted together, such that the same ternary metallic system is formed, along a laser path. Conclusions are drawn based on the fundamental R-T case and further explored in the more industrially relevant 3D PBF investigation. It is shown that the role of vapour bubble condensation within PBF processes is crucial in promoting mixing and chemical homogenisation in the fluid state; such insights are made possible by the rigorous mathematical description of the vapourisation/condensation process.

2. Method

To mathematically describe the multi-component system, experiencing fusion and vapourisation state transitions, a framework of partial differential equations is used to describe the conservation of momentum, the conservation of energy and the conservation of mass. The momentum conservation equation can be represented as:

$$\frac{\partial(\rho \boldsymbol{U})}{\partial t} + \nabla\cdot(\rho\boldsymbol{U}\otimes\boldsymbol{U}) = -\nabla P + \nabla\cdot\boldsymbol{\tau} + \boldsymbol{F_s} + \boldsymbol{F_g} + \boldsymbol{S_m} \tag{1}$$

where ρ, $\boldsymbol{U}$ and P are the mixture density, mass averaged velocity and pressure. The stress tensor, $\boldsymbol{\tau}$, is given by:

$$\boldsymbol{\tau} = \mu\left[\nabla\boldsymbol{U} + (\nabla\boldsymbol{U})^T\right] - \frac{2}{3}\mu(\nabla\cdot\boldsymbol{U})\boldsymbol{I}. \tag{2}$$

Here μ is the mixture-averaged kinematic viscosity. The source terms $\boldsymbol{F_g}$ and $\boldsymbol{S_m}$ in the momentum conservation equation describe the buoyancy forces and loss of momentum due to solidification of the substrate material within the flow respectively:

$$\boldsymbol{F_g} = \rho g\beta(T - T_L) \tag{3}$$

$$\boldsymbol{S_m} = K_1\frac{(1-\epsilon_1)^2}{\epsilon_1^3 + K_2}\boldsymbol{U} \tag{4}$$

where $\boldsymbol{g}$ is the gravitational acceleration vector, T_L is the mixture averaged liquidus temperature, and β is the thermal expansion coefficient. ϵ_1 is then the volume fraction of components in the fluid (liquid or vapour) states. In this work a simplified approach is used to estimate the solidus and liquidus temperatures for the multi-component flow. This involves linearly interpolating the melting temperatures for the pure substances present in any given region, weighted by the fraction of phase present, and applying a temperature range of 20 K with the solidus temperature taken as the lower bound and the liquidus as the upper bound of this range. The surface tension source is found by considering the interactions of all species locally present and their respective, pair-wise, surface tension coefficients, σ_{kl}:

$$\boldsymbol{F_s} = -\sum_{k=0}^{N}\sum_{l\neq k}^{N}\left[\sigma_{kl}\nabla\cdot\left(\frac{\boldsymbol{\psi}}{|\boldsymbol{\psi}|}\right)\left(\frac{\boldsymbol{\psi}}{|\boldsymbol{\psi}|}\right) + \frac{d\sigma_{kl}}{dT}\left(\nabla T - \frac{\boldsymbol{\psi}}{|\boldsymbol{\psi}|}\left(\frac{\boldsymbol{\psi}}{|\boldsymbol{\psi}|}\cdot\nabla T\right)\right)\right]|\boldsymbol{\psi}| \tag{5}$$

where $\boldsymbol{\psi} = \alpha_l\nabla\alpha_k - \alpha_k\nabla\alpha_l$., with $\sum_{k=0}^{N}\alpha_k = 1$. In this work we assume that the Dufour effect and Soret effect are negligible. It is further assumed that heat transport through species diffusion is negligible. With these assumptions, the heat transport equation for the mixture can be defined as:

$$\frac{\partial(\rho c_p T)}{\partial t} + \nabla \cdot (\boldsymbol{U} c_p \rho T) - \nabla \cdot (k \nabla T) = q + \boldsymbol{\tau} : \nabla \boldsymbol{U} - L_f \left[\frac{\partial(\rho \epsilon_1)}{\partial t} - \nabla \cdot (\boldsymbol{U} \epsilon_1 \rho) \right] - L_v \dot{m}_T \tag{6}$$

where c_p, T, and k are the mixture heat capacity, temperature, thermal conductivity respectively. L_f and L_v are the latent heats of fusion and vapourisation for the mixture. q is the heat input source representing the laser. In this work a surface Gaussian distribution is used with radius a_{laser}, as described elsewhere [27]. The mixture averaged properties of the flow are found by a weight fraction sum over the component properties as: $X = \sum_k \alpha_k X_k$ where X is the mixture averaged property to be found, X_k is the phase property of component k, and α_k is the volume fraction of component k, defined as the ratio of the volume of component k in a given cell to the total volume of all components in the cell; $\alpha_k = \frac{V_k}{\sum_j V_j}$. For the thermal conductivity and specific heat, this is further expanded to include the different property values in the solid and liquid state: $X = \sum_k (1 - \epsilon_1) \alpha_k X_{k,s} + \epsilon_1 \alpha_k X_{k,l}$. The final set of equations for the multi-component system are the species fraction transport equations:

$$\frac{\partial(\rho_k \alpha_k)}{\partial t} + \nabla \cdot (\rho_k \boldsymbol{U} \alpha_k) = \nabla \cdot \left(\rho D_k \nabla \left(\frac{\rho_k \alpha_k}{\rho} \right) \right) + \dot{m}_k. \tag{7}$$

In this work, the species present in the domain are decomposed further into condensed or vapourised/dispersed phases. This permits the vapourisation state transition to be properly captured for the multi-component substrate. $\dot{m}_k$ is then the production rate (positive and negative) of the k^{th} component in the system. For any given condensed phase, $\dot{m}_k$ is a source term for condensation processes, and a sink term for evaporation processes. In this work we use a simple description of $\dot{m}_k$ given by $\frac{r_{vap} \alpha_{liquid} \rho (T - T_{vap})}{T_{vap}}$ for vaporisation and $\frac{r_{cond} \alpha_{vapour} \rho (T_{vap} - T)}{T_{vap}}$ for condensation. $\dot{m}_k$ is set such that when a condensed component in a computational cell rises above its respective boiling temperature, the transition to the vapourised state occurs almost instantly - through setting $r_{cond/vap}$ approximately equal to the reciprocal of the time-step. It was found that the form of $\dot{m}_k$ did not affect the results significantly, provided the rapid vapourisation/condensation was captured. In this work, the maximum time-step size was limited to $1.0 \times 10^{-8} s$. Note that diffusion is only considered to occur in the liquid and vapour state. The effective diffusion coefficient D_k of the mixture is found from a weighted summation over the binary diffusion pairs, using a generalised Fickian model. It is assumed that the diffusion coefficients between condensed and vapourised phases is zero. In this manner, by neglecting diffusion between phases with radically different densities, it is reasonable to neglect the higher order diffusion terms from the $\nabla \cdot \left(\rho D_k \nabla \left(\frac{\rho_k \alpha_k}{\rho} \right) \right)$ expression in Eq. (7). The timescales involved in the processes of interest make these higher order terms negligible. Furthermore, these higher order terms are only relevant when considering diffusion between phases with large density contrast [29]. For the set of multi-component transport equations to be mass conserving, the sum over all phases should reproduce the continuity equation:

$$\underbrace{\sum_k \frac{\partial(\rho_k \alpha_k)}{\partial t}}_{\frac{\partial \rho}{\partial t}} + \underbrace{\sum_k \nabla \cdot (\rho_k \boldsymbol{U} \alpha_k)}_{\nabla \cdot (\rho \boldsymbol{U})} = \underbrace{\sum_k \nabla \cdot \left(\rho D_k \nabla \left(\frac{\rho_k \alpha_k}{\rho} \right) \right)}_{=0} + \underbrace{\sum_k \dot{m}_k}_{=0} \tag{8}$$

It will be shown that the present framework indeed conserves mass. The sum over the net production rate term, $\sum_k \dot{m}_k$, must be equal to zero, as physically the number of atoms present before and after a vapourisation or condensation event must be the same. It can be seen from expanding the total mass continuity equation that $\frac{\alpha_k}{\rho} \frac{D\rho}{Dt} = \alpha_k \nabla \cdot \boldsymbol{U}$, such a substitution reproduces the commonly known volume of fluid equation for the α_k phase, $\frac{\partial(\alpha_k)}{\partial t} + \nabla \cdot (\boldsymbol{U} \alpha_k) = \alpha_k \nabla \cdot \boldsymbol{U}$, with the addition of the mass transfer and diffusive terms. It can be interpreted that the $\dot{m}_k$ term describes the rate of change between the condensed and dispersed states of a given component, causing a localised density shift which is captured in the total derivative term, $\frac{D\rho}{Dt} = \frac{\partial \rho}{\partial t} + \boldsymbol{U} \cdot \nabla \rho$.

The governing equations are discretized using the OpenFOAM® library following the finite volume approach. The equations are evaluated in an iterative manner, correcting the velocity and pressure fields until convergence is reached, using a PISO (pressure implicit with splitting of operators) approach for multiple iterations at each time step. During the formation of the pressure-Poisson equation, the volumetric dilation due to vapourisation state transitions, $\dot{v}$, must be accounted for, so the pressure equation in the framework becomes:

$$\nabla \cdot \left(\frac{1}{A_D} \nabla p \right) = \nabla \cdot \phi - \frac{1}{\rho} \frac{D\rho}{Dt} \tag{9}$$

where $\frac{1}{A_D}$ are the diagonal entries of the momentum matrix equation and $\nabla \cdot \phi$ is the numerical equivalent of the divergence of the velocity field for a cell, taken at the cell faces. The volume dilation term, and multi-phase transport are handled explicitly; requiring extremely small Courant numbers. The multidimensional limiter for explicit solution (MULES) approach is utilised for the solution of the multi-component transport equation.

3. Results

In this section the proposed framework will first be applied to a fundamental multi-component mixing scenario in which the effect of inert gas entrainment in the fluid column, as well as entrainment of high temperature metallic vapour, is examined with respect to the effect on mixing and chemical homogenisation in the substrate. The framework will then be applied to an industrially relevant scenario of powder bed additive manufacturing using dissimilar metallic powders with the same compositions as the mixing case. In the powder AM scenario, the effect of heat input rate and beam radius is investigated and conclusions drawn on the more fundamental R-T instability predictions. Table 1 shows the thermo-physical parameters employed.

In both the fundamental mixing, and industrially relevant L-PBF scenarios presented, the mixing between two industrially relevant alloys. The first alloy has a volume fraction 0.64 Ni and 0.36 Fe (Invar). The second alloy has a volume fraction 0.5 Ni and 0.5 Ti (Nitinol). The Invar/Nitinol system then forms a ternary alloy system when diffusion and mixing between the two initial alloy compositions is considered. In all the presented cases, grid-dependency studies were performed via iterative grid-refinement. In all presented cases the control volumes are regular hexahedra.

3.1. On the effect of entrained multi-component vapour bubbles on the mixing dynamics of a dissimilar alloy system

It is well known that metallic vapour bubbles are often entrained within the liquid melt during additive manufacturing processes featuring high energy density heat sources. The effect of these bubbles on the mixing dynamics is poorly understood as their flow is difficult to measure and robust mathematical frameworks describing their evolution have proven evasive. As previously stated we consider the mixing of 2 initial binary alloys of Nitinol and Invar that form a ternary metallic system. Here we consider a scenario where the more dense Fe bearing alloy initially

Table 1
Thermo-Physical Properties used in the simulations. The thermal conductivities for the molten state, k_{liquid}, are estimated [30–33].

	Fe	Fe_{vapour}	Ni	Ni_{vapour}	Ti	Ti_{vapour}	Ar
ρ	7874	7.874	8908	8.908	4506	4.506	1.4
$\nu = \frac{\mu}{\rho}$	1×10^{-6}	5×10^{-6}	1×10^{-6}	5×10^{-6}	1×10^{-6}	5×10^{-6}	1.48×10^{-5}
k_{solid}	80.4	-	90.9	-	22	-	-
k_{fluid}	30.0	0.017	35.0	0.017	26.0	0.017	0.017
$c_{p_{solid}}$	456	-	450	-	523	-	-
$c_{p_{fluid}}$	820	820	730	440	550	350	521
T_{melt}	1810	-	1728	-	1940	-	83
T_{vap}	3134	3134	3000	3000	3560	3560	87
L_{fus}	2.7×10^5	-	2.97×10^5	-	2.96×10^5	-	-
L_{vap}	-	6.09×10^6	-	6.52×10^6	-	8.89×10^6	-
β	1×10^{-5}	5×10^{-5}	1×10^{-5}	5×10^{-5}	1×10^{-5}	5×10^{-5}	5×10^{-5}

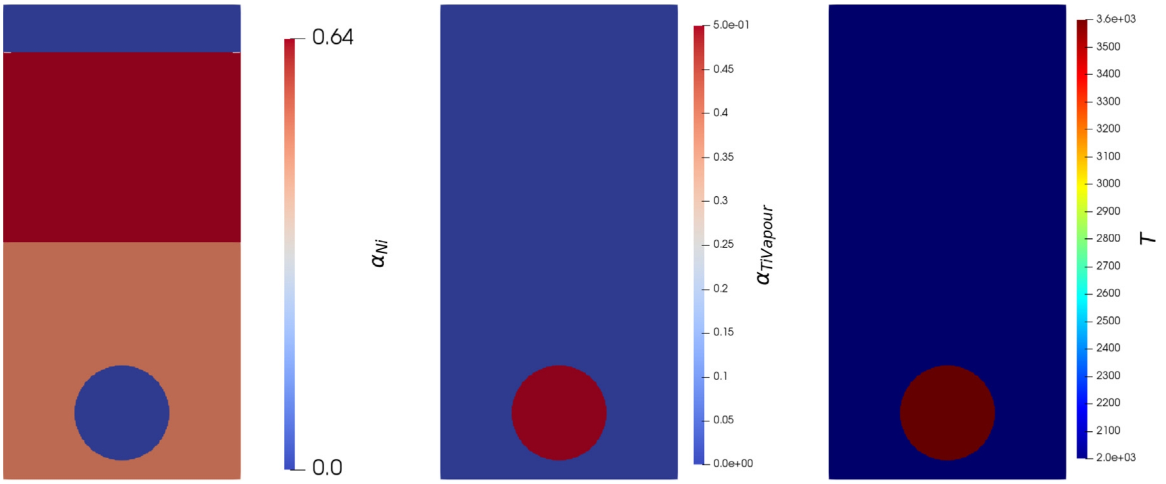

(a) Initial Nickel volume fraction (b) Initial Titanium vapour volume fraction (c) Initial temperature distribution

Fig. 1. Initial conditions for the vapour bubble Rayleigh-Taylor instability case. A metallic vapour bubble with a volume fraction of 0.5 Ni vapour and 0.5 Ti vapour is initialised at the base of the domain with an initial temperature of $3600\,K$. Note that in the Ar bubble case, the bubble is initialised at the same location and temperature as the vapour bubble case.

rests above the lighter alloy. This configuration, and the ensuing instability at the interface that precedes mixing, is commonly referred to as the Rayleigh-Taylor instability. In addition to the standard Rayleigh-Taylor case, we consider two additional scenarios; one in which a binary vapour bubble is present at the base of the domain and one in which this vapour bubble is replaced with an inert Ar bubble of the same size at the base of the fluid column, initialised at the same high temperature. Fig. 1 shows the initial conditions for the R-T vapour bubble scenario.

In each scenario a small random noise perturbation is initialised in the velocity field with magnitude $1 \times 10^{-9} ms^{-1}$. For all T and α_K boundaries a zero gradient condition is utilised. For velocity a slip boundary is applied at the vertical walls, with no-slip on the top and bottom walls of the domain. The domain size is $6 \times 10^{-3} m$ in the vertical direction and $3 \times 10^{-3} m$ in the horizontal direction; discretised into a regular grid of 1200×600 cells respectively. The radius of the bubbles initialised for the Ar and vapour bubble scenarios is $6 \times 10^{-4} m$.

It can be seen from Fig. 2 that both cases with entrained bubbles experience a greater degree of mixing than the reference case with no bubble. Also evident is that the reference case with no bubble takes a significantly longer amount of time for mixing to begin. Without the effect of a bubble rising through the interface between the two alloys it takes much longer for the instability to manifest. In both the vapour and Ar cases, the interface is disturbed much earlier. For the vapour case, it can be seen that the bubble is already significantly reduced in size due to condensation, even before reaching the interface. In both bubble cases, the rising vapour and Ar bubbles carry the lighter alloy through the interface, as this becomes entrained in their wake. Comparing the three scenarios at $t = 1s$, shown in Fig. 2, the vapour bubble case appears to be more mixed than the air bubble case. Fig. 3 shows a quantitative plot of the Ti volume fraction over a vertical line segment through the domain.

It can be seen from Fig. 3 that the vapour bubble case is indeed more homogenised than both the reference case, and crucially, the Ar bubble case. Therefore it is clear that the additional contribution to the momentum field caused by the condensation of the vapour bubble is significant to the flow development. This is interesting given that the vapour bubble condenses completely before breaking the liquid-metal/Ar boundary. In the Ar bubble scenario, the rising bubble does not decrease in size as it traverses, and once the bubble breaks the surface significant ripples are observed that enhance mixing. The prominent observation is that the vapour bubble case demonstrates more mixing than the Ar bubble case.

Although the mass conservation equation, $\frac{\partial \rho}{\partial t} + \nabla \cdot (\rho \boldsymbol{U}) = 0$, is not explicitly solved in the present framework, it is a consequence of the individual phase conservation equations as already discussed. Any numerical framework must be mass conservative for the fundamental assumptions of continuum mechanics to be valid, this is particularly important when state transitions involving changes in density are considered. Fig. 4 shows the numerical

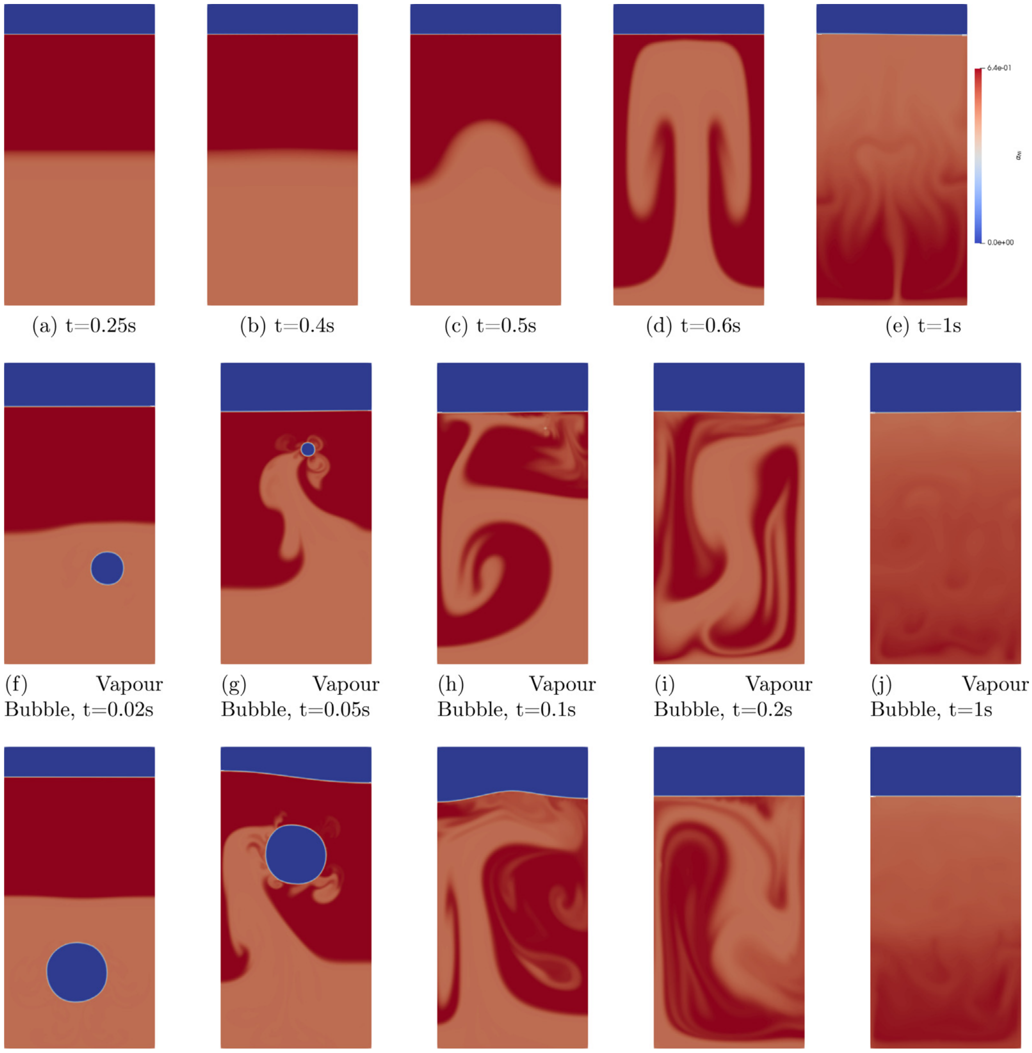

(a) t=0.25s (b) t=0.4s (c) t=0.5s (d) t=0.6s (e) t=1s

(f) Vapour Bubble, t=0.02s (g) Vapour Bubble, t=0.05s (h) Vapour Bubble, t=0.1s (i) Vapour Bubble, t=0.2s (j) Vapour Bubble, t=1s

(k) Ar Bubble, t=0.02s (l) Ar Bubble, t=0.05s (m) Ar Bubble, t=0.1s (n) Ar Bubble, t=0.2s (o) Ar Bubble, t=1s

Fig. 2. Evolution of the Ni volume fraction for the three Rayleigh-Taylor mixing scenarios considered. In the first scenario, panels a-e, a classical instability is considered due to a denser Invar alloy being present above a lighter one. Next the R-T configuration contains a metallic vapour bubble (1:1 Ni vapour:Tivapour) that condenses with time, as shown in panels (f–j). Finally the R-T case with a rising Ar bubble, panels (k–o), is shown.

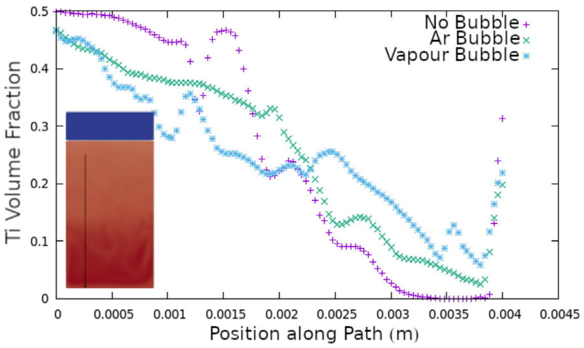

Fig. 3. Line plots for the Ti volume fraction along the path shown in the Figure, it can be seen that for the case where the vapour bubble was present, that the degree of chemical homogenisation is greater in the domain, as qualitatively appears to be the case in Fig. 2.

value of the mass conservation equation in the domain for the case where a binary vapor bubble is condensing and collapsing in the Rayleigh-Taylor configuration at $t = 0.02\,s$.

It can be seen from Fig. 4 that the framework is conservative of mass to machine accuracy, demonstrating the robustness of the framework and its numerical implementation.

3.2. L-PBF Within a ternary metallic system initially comprised of two dissimilar binary alloys

The high fidelity modelling framework is now applied to investigate a powder bed fusion process in which the powder used contains a mixture of two alloys; the same Invar and Nitinol alloys described in the previous section. A representative laser heat source is scanned across the top surface of this powder mixture, with differing beam radii and input power; from the simulations, conclusions are drawn regarding the effect of power density on mixing dynamics and final chemical heterogenisation following domain solidification. The powder particles are randomly sampled from the Gaussian distributions shown in Fig. 5(c) and positioned on the substrate through the application of a ”rain dropping” algorithm described in [25]. This involves calculating the path of a particle as it falls from height from a random location within the domain, encountering and moving around objects until the parti-

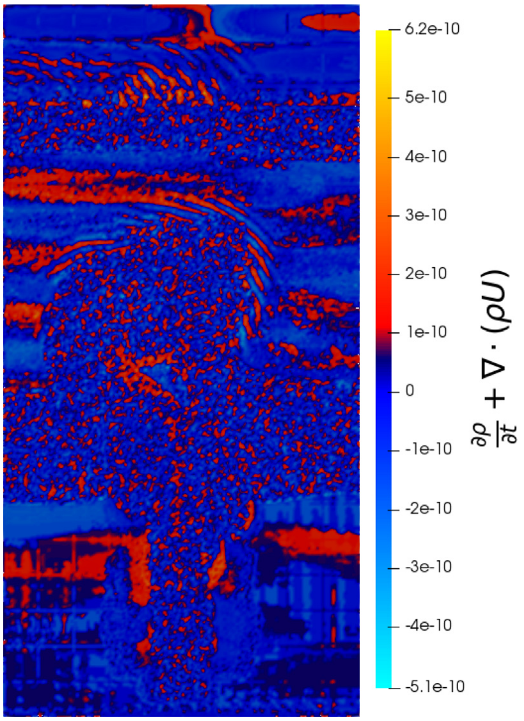

Fig. 4. Numerical value of the mass continuity equation at $t = 0.02s$ for the vapour bubble collapse scenario showing that the mass is conserved in the presented framework.

cle comes to rest on either the substrate surface, or the path to the substrate is blocked by other particles. This is approximately similar to the distribution of powder distribution seen in the topmost layer of a commercial L-PBF process. Two powders are mixed to form the initial conditions, as previously stated. The first powder is an alloy of Ni and Ti with a volume fraction of 0.5 for each component in these powder particles. The second powder is an alloy of Ni and Fe with a volume fraction of 0.64 for the Ni component in these powder particles with the remaining fraction being the Fe component. These two powders are randomly mixed to form the initial powder distribution used in the L-PBF simulations to form a 3-component system - Ni, Ti and Fe. The initial volume fractions of the components over the entire computational domain were 0.2206, 0.1345 and 0.1150 for the Ni, Ti and Fe respectively; where the remaining volume fraction is accounted for by the Ar component. Fig. 5 shows the initial distributions of the particles in the computational domain.

The computational domain utilised was $2.5 \times 10^{-4}m$ in the x-direction, $2.5 \times 10^{-4}m$ in the y-direction and $5 \times 10^{-4}m$ in the z-direction. The domain was discretised into 3,456,000 cells. Three scenarios were considered to determine the effect of laser spot diameter and power input on the mixing dynamics of the powder bed process. In all three scenarios, the laser travels along across the domain at $1.5ms^{-1}$. In scenario 1, the laser beam radius is $50 \times 10^{-6}m$, with a heat input Q of 140 W. In scenario 2, the same heat input of 140 W was used, but with the beam radius halved to $25 \times 10^{-6}m$. Finally in the third scenario, a beam radius of $25 \times 10^{-6}m$ was used, but this time with a heat input of 400 W. Note that commercial L-PBF systems intended for metals typically employ one or more lasers between 400 and 1000 W.

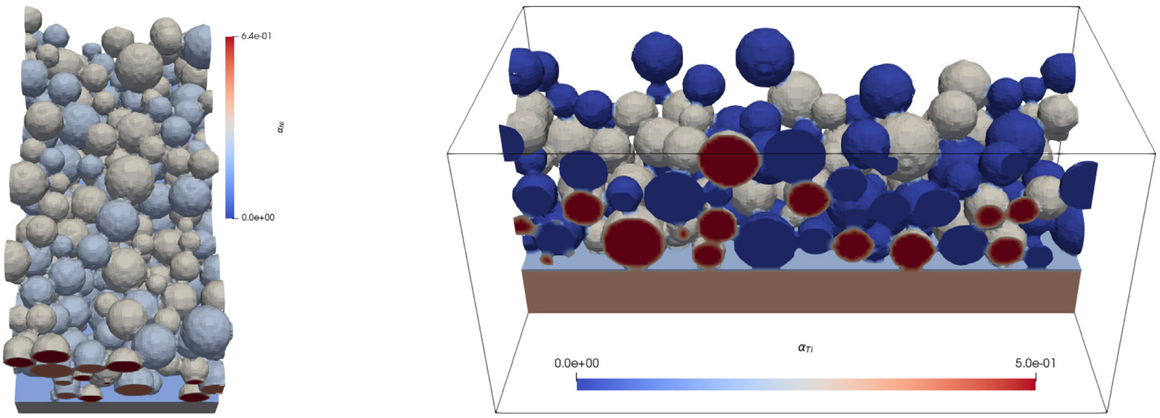

(a) Initial Nickel volume fraction

(b) Initial Titanium volume fraction

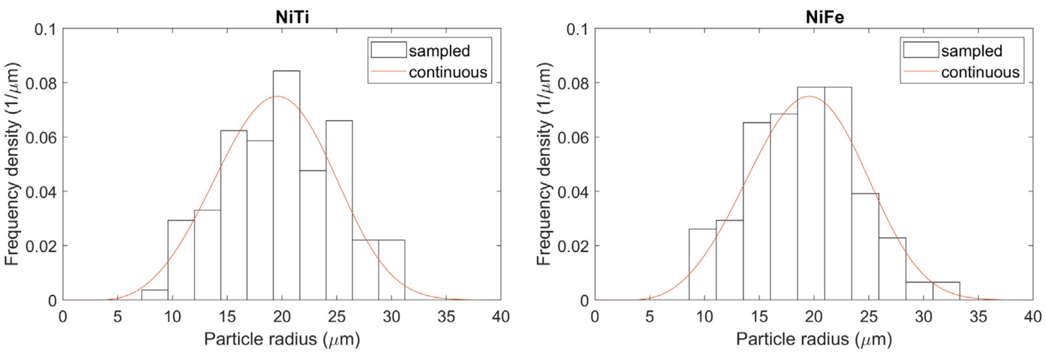

(c) Frequency density distributions for the two alloy powders considered in these simulations

Fig. 5. Initial component distributions in the domian for the laser powder bed scenarios.

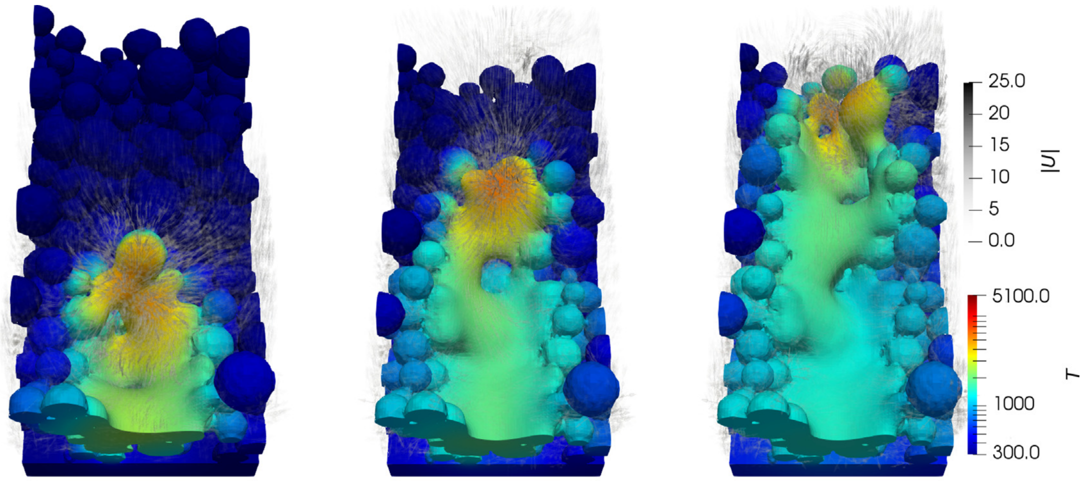

(a) Case 1, $t = 1 \times 10^{-4}\, s$ (b) Case 1, $t = 2 \times 10^{-4}\, s$ (c) Case 1, $t = 3 \times 10^{-4}\, s$

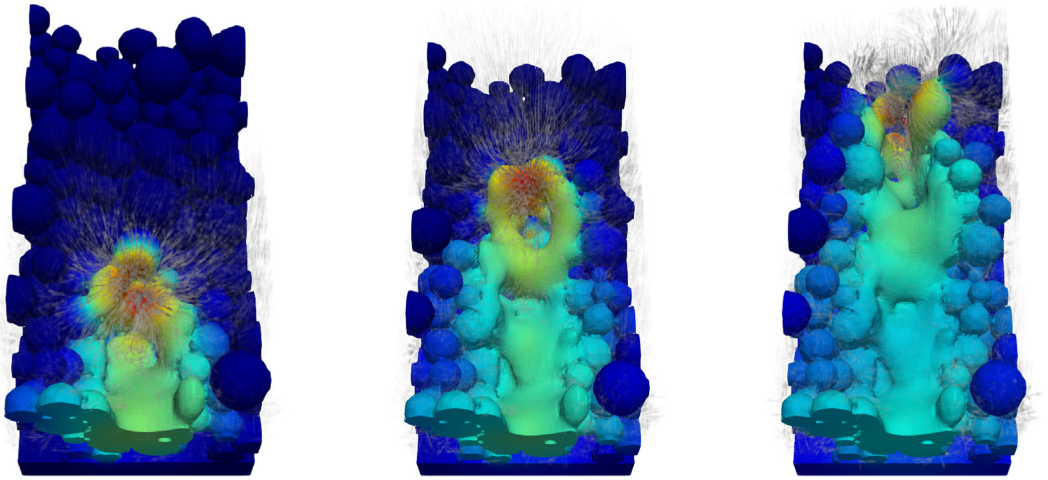

(d) Case 2, $t = 1 \times 10^{-4}\, s$ (e) Case 2, $t = 2 \times 10^{-4}\, s$ (f) Case 2, $t = 3 \times 10^{-4}\, s$

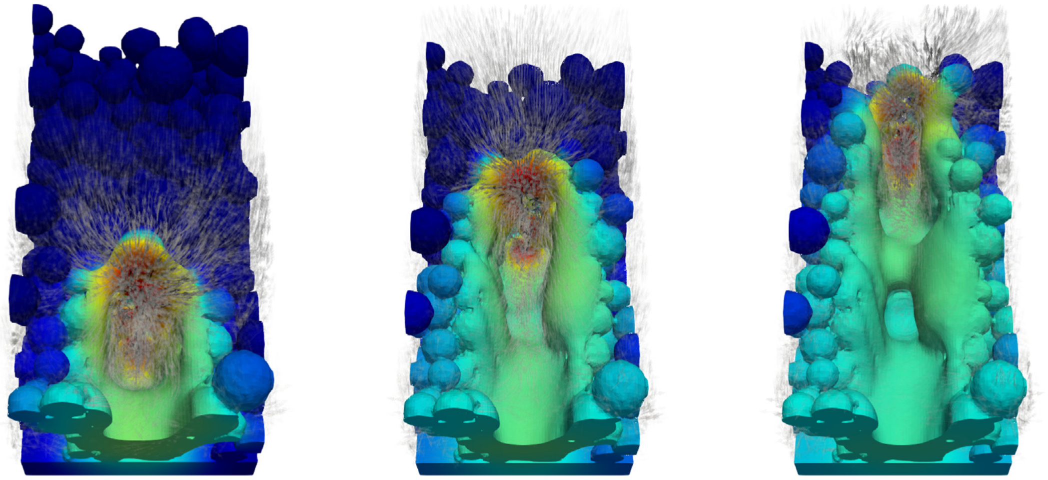

(g) Case 3, $t = 1 \times 10^{-4}\, s$ (h) Case 3, $t = 2 \times 10^{-4}\, s$ (i) Case 3, $t = 3 \times 10^{-4}\, s$

Fig. 6. Increasing the power density of the incident laser heat source causes significantly more melting, and causes a more stable thermo-capillary to be formed (Case 3). As the power density increases, more of the substrate material is vapourised, leading to increasing local velocity fields. In Case 1, the fluid velocity in the region of the heat source has a maximum velocity magnitude of 16ms^{-1}, in Case 2 this local maximum increases to 26ms^{-1}, and in Case 3, with significantly greater vapourisation induced, this local maximum in velocity reaches 56ms^{-1} in the vapour plume.

Table 2
Percentage losses for the three metallic species present in the L-PBF scenarios with increasing power density of the applied heat source.

	% Ni loss	% Ti loss	%Fe loss
Case 1	3.72×10^{-3}	1.39×10^{-3}	3.29×10^{-3}
Case 2	7.87×10^{-3}	2.11×10^{-3}	5.39×10^{-3}
Case 3	2.72×10^{-2}	9.72×10^{-3}	1.83×10^{-2}

Fig. 6 shows instances in time for the three scenarios considered. Note that in Fig. 6 the vapour, and Ar phases are rendered transparent so that only the solid and liquid states are visible, as would largely be the case experimentally.

It can be seen from Fig. 6 that as the power density of the laser is increased, both the local temperature, and local velocity magnitude around the heat source increase dramatically. Comparing scenarios 1 and 2 it can be seen that the molten-region is wider for the wider-beam case, although the peak temperature in the molten region is lower in magnitude, which is as expected. For scenario 3, where the beam is narrow, and the heat input also high at 400W, it can be seen that the penetration depth of the thermo-capillary is considerably greater that the other two scenarios. For scenarios 1 and 2 the power density is insufficient to generate any meaningful thermo-capillary. As the temperature gradient across the liquid/vapour interface increases, so too does the magnitude of the tangential surface flows, driven by the gradient of surface tension with temperature - commonly referred to as the Marangoni effect. The higher magnitude velocity field induced in scenario 3 is largely due to the combination of Marangoni effects, and the large volumetric dilation due to the vapourisation of the substrate - this vapourisation induces a recoil-like effect at the liquid/vapour interface. It can be seen in Fig. 6(g–i) that after the material flows away from the heat source location (due to Marangoni and recoil driven flow), normal surface tension, and gravity effects become dominant and the liquid material begins to flow back down into the domain, pursued by a solidification front that will eventually freeze the flow. It can be seen in Fig. 6(i) that after the heat source passed the center of the powder bed, the two lobes of liquid metal that were pushed out of the channel on either side were pulled back down by a combination of gravity and surface tension, and formed a metallic ligament across the central scan-line.

Fig. 7 shows a cross section through the domain, for the three scenarios following solidification of the melt track, at $t = 6 \times 10^{-4}s$, with the volume fraction of the Ti component plotted.

It can be seen from Fig. 7 that as the power density increased, the degree of chemical homogenisation along the laser path increased. The effect of the Marangoni flow in the substrate is also clear when comparing Fig. 7(a) and (b), as can be seen in the more aggressive changes in the surface profile of the narrower beam scenario (generated by larger transverse surface velocities away from the laser heat source). For scenario 3, it can be seen that the thermo-capillary extended through the entire powder bed, and even melted the base substrate material, whereas for the lower power scenarios the substrate plate did not experience any melting.

It is interesting to consider the effect of the heat source on the composition of the substrate, and to what degree the various elements have been lost from the domain due to the vapourisation of the substrate. Table 2 shows the percentage losses for the various chemical elements present in the simulations for the three scenarios considered.

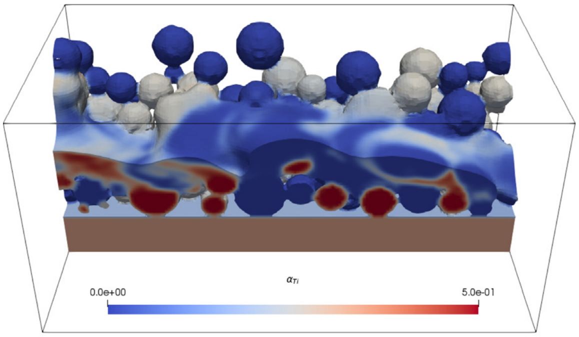

(a) Case 1

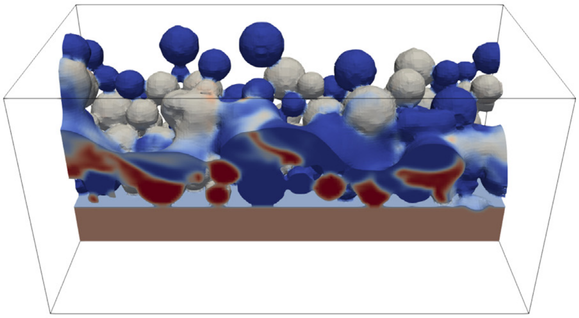

(b) Case 2

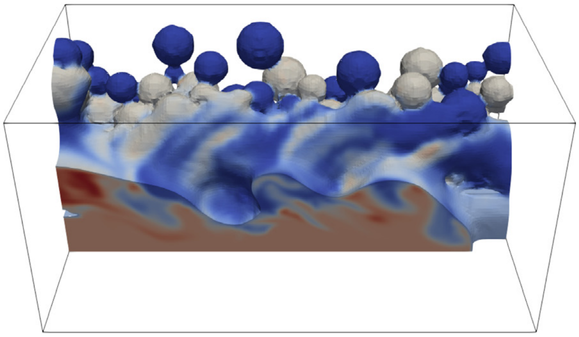

(c) Case 3

Fig. 7. Volume fraction of the Ti component following solidification of all three power density scenarios. As the power density is increased, more of the metallic substrate is vapourised leading to increased velocity fields due to Marangoni flow and the recoil effect explicitly due to vapourisation. The overall effect of greater vapourisation is to induce greater chemical homogenisation.

It can be seen from Table 2 that as the power density of the applied heat source is increased (Case 1 → Case 2 → Case 3), the amount of metallic material lost from the computational domain increases for all components. This loss of material is due to the vapourisation of these components and subsequent ejection from the domain out of the top boundary. This has been treated as an open-container boundary condition.The obtained quantitative measure of the increase in vapourisation, or 'keyholing', is in agreement with the behaviour seen in Fig. 6. In all scenarios, it is the Ni component that has the largest mass loss, followed by Fe and then Ti. Knowledge of the vapourisation temperatures of the three species goes some way to explaining this, with Ni having the lowest vapourisation temperature, followed by Fe and then Ti. However, it is interesting to observe that the rate of increase in mass loss is not linear with respect to increasing power density.

4. Discussion

The utilisation of a more physically robust modelling framework, that fully captures the volumetric dilation during the vapourisation/condensation transitions ($\frac{1}{\rho}\frac{D\rho}{Dt} = \nabla \cdot \boldsymbol{U}$), as well as the multi-component nature of the L-PBF process ensures a more complete physical description of such processes are obtained; this robust approach gives confidence in the numerical results presented, over other approaches that do not contain all of the physics. The modelling framework can accelerate the design of novel MM-FGAM applications by determining suitable parameters that can either mitigate or promote mixing. In power beam welding applications, it is known that there are significant differences in chemistry in the regions that keyholing occurs, often resulting in an undesirable heterogeneous response unless a stable keyhole is consistently achieved. Therefore, the presented modelling framework can assist in identifying a set of beam characteristics that predict stable keyhole formation.

In the present L-PBF scenarios considered, it is shown that as the power density of the applied heat source increases, the proportion of vapourised substrate material also increases; although the rate of increase in elemental loss is different for each chemical component in the domain. For the cases considered, the total mass loss from the substrate due to vapourisation was smaller than would have been observed for a process such as electron beam joining, where the power density is significantly higher. It is further observed that increasing the power density promotes increased melting and vapourisation, which in turn leads to significantly greater chemical homogenisation. These observations can be further informed from the Rayleigh-Taylor studies, where it is shown that condensing metallic vapour significantly increases the mixing between components. We see in the L-PBF scenarios that as the power density increases, chemical components in the domain are lost preferentially as a function of their relative vapourisation temperatures. The percentage losses of each component do not increase at the same rate as the power density is increased, and therefore it is possible to extrapolate that with even greater power density, a threshold will be reached where undesirable chemical heterogenisation due to preferential element evaporation is induced in the L-PBF substrate. It is important to be able to obtain accurate predictions of substrate chemistry, as this chemistry often governs the precipitation kinetics in the material and,along with the thermal history, largely determines the strength of the material. The current approach uses a simplified mixture approximation for the material properties based on the component volume fractions. In the future the authors intend to use thermodynamic approaches to obtain the mixture properties (e.g. $T_{solidus}$, $T_{liquidus}$, thermal conductivity, specific heat, viscosity) as a function of temperature and composition. This thermodynamic parameter determination will further improve the presented framework. Additionally, in this work, we assume that the density ratio between all condensed and vapourised states is 1×10^3. In the future it is planned to implement the vapourisation density change as a function of local super-heating, or implement a fully compressible approach with equation of state.

5. Conclusions

A high fidelity mathematical modelling framework has been developed and applied to understand, and quantify, the role of metallic vapour on the mixing dynamics and chemical homogenisation in L-PBF processes. The novelty in the mathematical framework lies in explicitly solving a series of pairs of component fraction transport equations (one for the condensed and one for the vapourised states of each chemical element in the domain) with source and sink terms to accurately capture mass transfer between liquid and vapour states (per-component). Coupled with the proper treatment of this transition between condensed and vapourised states, through the generation of a volumentric dilation term in the closure relation that captures the flow response due to the step change in density during transitions, this explicit treatment of the chemical constituents permits the fluid dynamics of the system to be fully captured numerically for the first time. This permits high fidelity investigations into the material behaviour when subjected to high energy density sources of heat. Using the framework, initially a fundamental study was performed into the role of a condensing vapour bubble, compared with an inert Ar bubble, on the mixing of dissimilar binary alloys in a Rayleigh-Taylor instability scenario. It is shown that a condensing vapour bubble promotes a greater degree of mixing compared with the analogous non-condensing Ar scenario due to the additional momentum contributions due to condensation. The framework is then applied to study a L-PBF process considering the same two dissimilar alloys, as powders, with increasing power density of the applied laser heat source. It is shown that as the power density increases, the lower vapourisation temperature elements are preferentially evaporated from the domain. Interestingly, the rate at which these elements are lost as the power density increases, is different for each component. Using the results from the fundamental Rayleigh-Taylor scenarios it is possible to glean further understanding from the L-PBF simulations and conclusively state that the role of vapour condensation in the proportion of mixing is important aspect of this process, and to capture this in a high fidelity, robust modelling approach is needed. In summary:

1. Entrained vapour bubbles in liquid metals promote greater mixing than inert bubbles due to the additional momentum flux that is generated during condensation.
2. Higher power density in the L-PBF process generates a greater melt-volume in the substrate and larger magnitude velocity fields which aid in chemical homogenisation.
3. An increase in the applied power density in the L-PBF process promotes a greater degree of vapourisation.
4. The increase in component loss is not uniform as the power density increases in L-PBF, suggesting that at some threshold, chemical heterogenisation will always occur, and is inherent in the process.

Data availability

The authors declare that the data supporting the findings of this study are available from the corresponding author upon reasonable request.

Declaration of Competing Interest

The authors declare there are no conflicts of interest, including any financial, personal or other relationships with other people or organizations within three years of beginning the submitted work that could inappropriately influence or be perceived to influence, the work.

CRediT authorship contribution statement

T.F. Flint: Conceptualization, Formal analysis, Investigation, Methodology, Project administration, Resources, Software, Visualization, Writing – original draft, Writing – review & editing. **M.J. Anderson:** Conceptualization, Formal analysis, Software, Writing – original draft, Writing – review & editing. **V. Akrivos:** Conceptualization, Writing – review & editing. **M.J. Roy:** Writing – original draft, Writing – review & editing. **J.A. Francis:** Project administration, Resources, Writing – original draft, Funding acquisition. **A. Vasileiou:** Funding acquisition. **M.C. Smith:** Funding acquisition, Project administration, Resources, Writing – original draft.

Acknowledgments

The work presented in this manuscript is supported by the Engineering and Physical Sciences Research Council (EPSRC) under the “Cobalt-free Hard-facing for Reactor Systems” grant EP/T016728/1.

The authors would like to acknowledge the assistance given by IT Services and the use of the Computational Shared Facility at The University of Manchester.

References

[1] W.E. King, A.T. Anderson, R.M. Ferencz, N.E. Hodge, C. Kamath, S.A. Khairallah, A.M. Rubenchik, Laser powder bed fusion additive manufacturing of metals; physics, computational, and materials challenges, Appl. Phys. Rev. 2 (4) (2015) 041304.

[2] D.C. Hofmann, S. Roberts, R. Otis, J. Kolodziejska, R.P. Dillon, J.-o. Suh, A.A. Shapiro, Z.-K. Liu, J.-P. Borgonia, Developing gradient metal alloys through radial deposition additive manufacturing, Sci Rep 4 (2014) 5357, doi:10.1038/srep05357. 165 citations

[3] H.C. Basoalto, C. Panwisawas, Y. Sovani, M.J. Anderson, R.P. Turner, B. Saunders, J.W. Brooks, A computational study on the three-dimensional printability of precipitate-strengthened nickel-based superalloys, Proceedings of the Royal Society A: Mathematical, Physical and Engineering Sciences 474 (2220) (2018) 20180295, doi:10.1098/rspa.2018.0295.

[4] J. Yin, W. Zhang, L. Ke, H. Wei, D. Wang, L. Yang, H. Zhu, P. Dong, G. Wang, X. Zeng, Vaporization of alloying elements and explosion behavior during laser powder bed fusion of cu-10zn alloy, Int. J. Mach. Tools Manuf 161 (2021) 103686, doi:10.1016/j.ijmachtools.2020.103686 .

[5] Y. Qin, P. Wen, H. Guo, D. Xia, Y. Zheng, L. Jauer, R. Poprawe, M. Voshage, J.H. Schleifenbaum, Additive manufacturing of biodegradable metals: current research status and future perspectives, Acta Biomater 98 (2019) 3–22, doi:10.1016/j.actbio.2019.04.046. 10th BIOMETAL2018 - International Symposium on Biodegradable Metals, https://www.sciencedirect.com/science/article/pii/S1742706119302892

[6] Y. Hu, S. Wu, P. Withers, J. Zhang, H. Bao, Y. Fu, G. Kang, The effect of manufacturing defects on the fatigue life of selective laser melted ti-6al-4v structures, Materials & Design 192 (2020) 108708, doi:10.1016/j.matdes.2020.108708.

[7] D.A. Chinakhov, E.G. Grigorieva, E.I. Mayorova, S.A. Solodsky, V.F. Torosyan, Dependence of manganese content in the weld metal on the velocity of active shielding gas flow, in: Conf. Ser. Mater. Sci. Eng., IOP, 2017.

[8] W. Yan, W. Ge, Y. Qian, S. Lin, B. Zhou, W.K. Liu, F. Lin, G.J. Wagner, Multi-physics modeling of single/multiple-track defect mechanisms in electron beam selective melting, Acta Mater. 134 (2017) 324–333, doi:10.1016/j.actamat.2017.05.061.

[9] K. Chongbunwatana, Simulation of vapour keyhole and weld pool dynamics during laser beam welding, Prod. Eng. 8 (4) (2014) 499–511, doi:10.1007/s11740-014-0555-x.

[10] J. Svenungsson, I. Choquet, A.F. Kaplan, Laser Welding Process - A Review of Keyhole Welding Modelling, Physics Procedia, 2015, doi:10.1016/j.phpro.2015.11.042.

[11] C.L. Qiu, C. Panwisawas, R.M. Ward, H.C. Basoalto, J.W. Brooks, M.M. Attallah, On the role of melt flow into the surface structure and porosity development during selective laser melting, Acta Mater. 96 (2015) 72–79.

[12] T. Flint, C. Panwisawas, Y. Sovani, M. Smith, H. Basoalto, Prediction of grain structure evolution during rapid solidification of high energy density beam induced re-melting, Materials & Design 147 (2018) 200–210, doi:10.1016/J.MATDES.2018.03.036.

[13] M. Courtois, M. Carin, P. Le Masson, S. Gaied, M. Balabane, A complete model of keyhole and melt pool dynamics to analyze instabilities and collapse during laser welding, J. Laser Appl. (2014), doi:10.2351/1.4886835.

[14] T.F. Flint, Y.L. Sun, Q. Xiong, M.C. Smith, J.A. Francis, Phase-Field simulation of grain boundary evolution in microstructures containing second-phase particles with heterogeneous thermal properties, Sci. Rep. 9 (1) (2019) 18426, doi:10.1038/s41598-019-54883-8.

[15] C.L.A. Leung, S. Marussi, R.C. Atwood, M. Towrie, P.J. Withers, P.D. Lee, *In situ* X-ray imaging of defect and molten pool dynamics in laser additive manufacturing, Nat. Commun. (2018), doi:10.1038/s41467-018-03734-7.

[16] O. Lopez-Botello, U. Martinez-Hernandez, J. Ramírez, C. Pinna, K. Mumtaz, Two-dimensional simulation of grain structure growth within selective laser melted AA-2024, Mater. Des. 113 (2017) 369–376, doi:10.1016/j.matdes.2016.10.031.

[17] C.L.A. Leung, S. Marussi, M. Towrie, R.C. Atwood, P.J. Withers, P.D. Lee, The effect of powder oxidation on defect formation in laser additive manufacturing, Acta Mater. (2019), doi:10.1016/j.actamat.2018.12.027.

[18] L. Aucott, H. Dong, W. Mirihanage, R. Atwood, A. Kidess, S. Gao, S. Wen, J. Marsden, S. Feng, M. Tong, T. Connolley, M. Drakopoulos, C.R. Kleijn, I.M. Richardson, D.J. Browne, R.H. Mathiesen, H.V. Atkinson, Revealing internal flow behaviour in arc welding and additive manufacturing of metals, Nat. Commun. (2018), doi:10.1038/s41467-018-07900-9.

[19] M. Bayat, W. Dong, J. Thorborg, A.C. To, J.H. Hattel, A review of multi-scale and multi-physics simulations of metal additive manufacturing processes with focus on modeling strategies, Addit. Manuf. 47 (2021) 102278, doi:10.1016/j.addma.2021.102278.

[20] M. Bayat, S. Mohanty, J.H. Hattel, A systematic investigation of the effects of process parameters on heat and fluid flow and metallurgical conditions during laser-based powder bed fusion of ti6al4v alloy, Int J Heat Mass Transf 139 (2019) 213–230, doi:10.1016/j.ijheatmasstransfer.2019.05.017.

[21] C. Panwisawas, C.L. Qiu, Y. Sovani, J.W. Brooks, M.M. Attallah, H.C. Basoalto, On the role of thermal fluid dynamics into the evolution of porosity during selective laser melting, Scr. Mater. 105 (2015) 14–17.

[22] L. Cao, Mesoscopic-scale simulation of pore evolution during laser powder bed fusion process, Comput. Mater. Sci 179 (2020) 109686, doi:10.1016/j.commatsci.2020.109686.

[23] M. Courtois, M. Carin, P. Le, Modelling of high-density laser -material.

[24] T.F. Flint, G. Parivendhan, A. Ivankovic, M.C. Smith, P. Cardiff, Beamweldfoam: numerical simulation of high energy density fusion and vapourisation-inducing processes, SoftwareX 18 (2022) 101065, doi:10.1016/j.softx.2022.101065.

[25] C. Panwisawas, C. Qiu, M.J. Anderson, Y. Sovani, R.P. Turner, M.M. Attallah, J.W. Brooks, H.C. Basoalto, Mesoscale modelling of selective laser melting: thermal fluid dynamics and microstructural evolution, Comput. Mater. Sci. 126 (2017) 479–490.

[26] M. Courtois, M. Carin, P.L. Masson, S. Gaied, M. Balabane, A new approach to compute multi-reflections of laser beam in a keyhole for heat transfer and fluid flow modelling in laser welding, J. Phys. D Appl. Phys. 46 (2013) 505305.

[27] T. Flint, L. Scotti, H. Basoalto, M. Smith, A thermal fluid dynamics framework applied to multi-component substrates experiencing fusion and vaporisation state transitions, Commun. Phys. 3 (1) (2020), doi:10.1038/s42005-020-00462-7.

[28] J. Shinjo, C. Panwisawas, Digital materials design by thermal-fluid science for multi-metal additive manufacturing, Acta Mater 210 (2021) 116825, doi:10.1016/j.actamat.2021.116825.

[29] S. Hosseini, N. Darabiha, D. Thãvenin, Mass-conserving advection-diffusion lattice boltzmann model for multi-species reacting flows, Physica A 499 (2018) 40–57, doi:10.1016/j.physa.2018.01.034.

[30] CRC Handbook of Chemistry and Physics: a Ready-Reference Book of Chemical and Physical Data, Choice Reviews Online (2010), doi:10.5860/choice.47-3553.

[31] J. Dean, Lange'S handbook of chemistry, 15th ed, 1999.

[32] Y. Zhang, J.R. Evans, S. Yang, Corrected values for boiling points and enthalpies of vaporization of elements in handbooks, J. Chem. Eng. Data (2011), doi:10.1021/je1011086.

[33] I. Mills, R. Jones, Quantities, units and symbols in physical chemistry, Vib. Spectrosc. (1990), doi:10.1016/0924-2031(90)80016-w.